



Cite this: DOI: 10.1039/c9an01869g

Single point single-cell nanoparticle mediated pulsed laser optoporation†

Sergiy Patskovsky,  * Mengjiao Qi and Michel Meunier 

This article presents an optical platform for studying the dynamics of nanoparticle assisted pulsed laser optoporation of individual living cells. Here plasmonic nanoparticles (NPs) act as markers of the exact spatial position of living cell membranes and as an enhancer for localized pulsed laser perforation. High contrast NP imaging using reflected light microscopy (RLM) allows accurate and automatic laser targeting at individual NPs for spatially controlled laser optoporation of single cells at a single point. The NP imaging method is compatible with fluorescence microscopy and a cellular incubator that allows study of real-time perforation kinetics of live cells and the optomechanical interaction of NPs with membranes. These parameters are of great interest for the development and experimental implementation of the technology of pulsed laser optoporation and transfection applied to single living cells as well as to bulk-level assays.

Received 20th September 2019,
Accepted 31st October 2019

DOI: 10.1039/c9an01869g

rsc.li/analyst

Introduction

Development of technologies that allow investigating different aspects of molecular dynamics at the single cell level¹ is of great importance for cancer diagnosis, classification, and treatment.² Such technologies should provide the possibility to study cell-to-cell variation in a population, analyze sub-cellular biological structures and also allow transfection at the single-cell level. Quantitatively controlled delivery of genetic modification substances into single cells requires the application of advanced bio-nanoengineering techniques for precise cellular membrane perforation. Multiple physical methods can achieve bulk cell transfection using mechanical, electrical, acoustic and optical approaches.^{3–6} Among them, the optoporation technique, based on laser-induced cell membrane perforation, is one of the most precise and accurate.^{7,8} Using precisely controlled laser-microscope system point-directed optoporation and transfection allows elucidation of distinct responses during cell optoporation and genetic modification at the single-cell level.⁷ The number and size of optoporated holes on the cell membrane as well as their precise spatial positions at the subcellular level can be controlled, which is usually not possible by conventional electroporation or sonoporation. Although competing technologies like the microinjection technique⁹ or single-cell electroporation¹⁰ can in principle be

adapted for single cell reagent delivery, these systems will be significantly more complicated to use.¹¹ An essential part of the optical transfection protocol is an initial cellular membrane optoporation that generally uses pulses from a tightly focused laser to puncture the cellular membrane at a single point. In this case, cell survival depends on the applied laser power and very importantly focalization precision. In spite of all technological advancements, laser-assisted methods still suffer from low targeting precision in the z-direction, which impacts the optoporation efficiency of the cellular membrane and can be considered as the main limitation for single-cell level transfection. Several approaches exist to circumvent this limitation by employing hardware, imaging and software algorithms and their combinations. For example, a height map of samples can be generated before optoporation¹² using numerical treatment of microscopy images. An optically trapped single gold nanoparticle (NP) placed at a controlled fixed distance from the substrate¹³ improves the reliability of cell perforation by laser-induced NP breakdown. The exact location of the cell membrane can also be detected by translating the optically trapped microparticle to the membrane surface.¹⁴ However, the common feature of all these techniques is the very high complexity of experimental realization. In this work, we propose an optical system for precise laser-induced nanoparticle-mediated single point optoporation of single cells. 100 nm plasmonic Au NPs deposited on the cell membrane serve as the markers of the exact spatial position of the cellular membrane. As they also provide an enhancement factor for local perforation performed by a tightly focused pulsed laser, localized membrane optoporation can be performed. Experimentally, a pulsed laser focal position is automatically

Engineering Physics Department, Ecole Polytechnique de Montréal, Laser Processing and Plasmonics Laboratory, Montréal, Québec, H3C 3A7, Canada.

E-mail: sergiy.patskovsky@polymtl.ca

† Electronic supplementary information (ESI) available. See DOI: 10.1039/c9an01869g

aligned with plasmonic NPs placed on the cellular membrane for consecutive illumination and local optoporation. To provide reliable identification and spatial localization of NPs in the cell environment, we adapted an imaging solution based on reflected light microscopy (RLM).¹⁵ This imaging approach uses a high numerical aperture (NA) objective which, when combined with rapid Gaussian algorithms for high-resolution 2D¹⁶ and 3D¹⁷ single-particle localization in a cellular environment, ensures fast and precise 3D NP mapping. RLM is based on NP backscattering detection and is thus compatible with an inverted microscopy setup equipped with fluorescence mode and a portable cellular incubator. What is also important, this setup can adapt a microfluidic system for single-cell separation and trapping¹⁸ and automatically targeted multiple cells for analysis. In this article, we present and discuss the results for opto-mechanical laser-NP interaction and provide a preliminary analysis of spatially controlled perforation of a single cell membrane by evaluating the kinetics of live-cell responses by real-time local fluorescence imaging.

Experimental

Cell culture and nanoparticle markers

Human MDA-MB-231 breast cancer cell lines (American Type Culture Collection, Manassas, VA, USA) were cultured at 5000 cells per cm² in cell culture-treated polystyrene T75 flasks (Sarstedt, Saint-Léonard, QC, Canada). Cells were grown in DMEM supplemented with 10% FBS and antibiotics (100 units per mL penicillin and 100 µg mL⁻¹ streptomycin, 1% PS) in a humidified incubator at 37 °C under a 5% CO₂ atmosphere. Confluent cells were removed by trypsinization and seeded for experiments in DMEM supplemented with 10% FBS/1% PS. Cells were seeded onto 19.625 cm² glass bottom dishes (5000 cells per cm², MatTek, Ashland, MA, USA). At 85% confluence, cells were washed once with PBS before adding NPs diluted to 8 µg mL⁻¹ in DMEM/10% FBS/1% PS. After 3 h of incubation at 37 °C, cells were washed three times with PBS.

To work as cellular membrane spatial position markers plasmonic NPs should remain on the cell membrane and not be internalized. It is known from the literature that NP uptake is size dependent and cells can endocytose NPs up to a few 100 nanometers with an optimum at 50 nm.¹⁹ However, it is not obvious that larger NPs^{20,21} (>50 nm) are able to penetrate and cross the membrane in early endosomes and can be concluded that they most probably stay on the membrane periphery.²² In this work, to target the cellular membrane we use 100 nm NPs in order to prevent cellular internalization and also provide increased backscattering intensity for a reliable optical detection. Further in the article, we present experimental results on the cellular uptake of NPs. AuNPs (50 µg mL⁻¹, 100 nm in diameter, A11-100-CIT) were purchased from Nanopartz (Loveland, CO, USA). Citrate-capped AuNPs were stored at 4 °C in the dark to minimize photoinduced oxidation.

The perforation kinetics of the cells was analyzed using the inflow dynamics of propidium iodide (PI) (Thermo Fisher Scientific), which was added to the cell medium at a concentration of 1.5 µM. PI, a membrane impermeable dye with a molecular weight of 670 Da, becomes fluorescently detectable upon binding to nucleic acids. Due to its extremely small size compared to the cell, PI enables isotropic inflow at the site of perforation and allows for the temporal and spatial investigation of the optoporation process. Calcein-AM (Thermo Fisher Scientific) with a concentration of 1 µM was used for the cell-viability assays after laser-induced perforation.

Microscopy setup for cell-NP imaging and NP-mediated laser perforation

The experimental system for single point single cell optoporation is schematically shown in Fig. 1. It was built on the basis of an inverted Eclipse Ti microscope (Nikon, Mississauga, ON, Canada) equipped with a 100× oil immersion objective (variable numerical aperture NA = 0.5–1.3). Glass-bottom dishes containing the cell cultures were placed in a cellular incubator system (Live Cell Instrument, Korea) installed on a flat top inverted microscope motorized stage (H117P1, ProScan, Prior Scientific, Rockland, MA, USA) which allowed for fine 3D spatial sample positioning. A fluorescent lamp C-HGFI Intensilight (Nikon) with an ET-DsRED excitation filter (545 ± 15 nm) (Chroma Technology, Bellows Falls, VT, USA 49005 – ET – DSRed (TRITC/Cy3)) provided light for NP-cell complex visualization with a QIClick digital CCD camera (QImaging, Surrey, BC, Canada) and for PI fluorophore excitation. In order to eliminate *switching* filter effects on the detection of the real-time kinetics, fluorescence imaging was performed by using an additional CCD camera (Hamamatsu R2) equipped with the corresponding emission filter (620 ± 30 nm for PI). Calcein dye was detected using appropriate filter sets (Chroma Technology, 49003 – ET – EYFP).

For the NP-mediated optoporation experiments described here, we used an ultra-compact 15 ns laser (QC532,

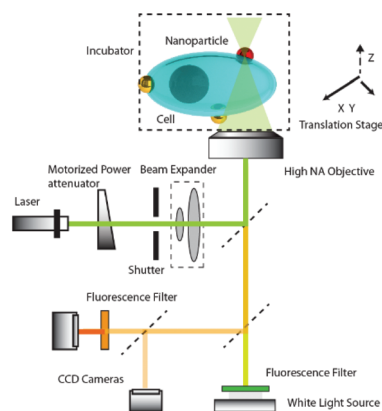


Fig. 1 Schematic representation of the experimental setup for single cell optoporation. Gold nanoparticles serve as markers of the live cell membrane position and an enhancement factor for local pulsed-laser optoporation.

CrystaLaser, USA) working at 100 Hz pulse frequency and 532 nm wavelength. The applied laser power on the sample was controlled by using home-made LabView software through the rotation of a half-wavelength waveplate combined with a plate polarizer on the beam path. The number of pulses of the ns-laser was selected by setting the open duration of a fast mechanical shutter (Thorlabs). A beam expander and a diaphragm were used to adjust the laser focal spot size by changing the effective numerical aperture. Three plate beam splitters were used in the setup for illumination and imaging. A laser beam delivery was provided by a 10 : 90 beamsplitter, and wide field NP imaging and fluorescence were separated by using a 50 : 50 beamsplitter ratio. A standard white light source (Nikon) with a 50 W halogen lamp was applied for conventional transmission microscopy and 3D imaging with oblique illumination.

Results and discussion

Wide-field RLM NP imaging in the cellular environment

Successful experimental realization of our proposed approach requires precise 3D spatial localization of individual NPs attached to the cell membrane. Such localization is made available by the combination of the mechanical 3D translation stage with the RLM optical approach for wide-field NP imaging in a diffusing environment.¹⁵ Two main factors explain the higher NP contrast in the cell–NP complex for RLM imaging as compared to conventional dark-field microscopy. First is that backscattering enhances NP–cell contrast due to the dominant Rayleigh scattering of NPs and highly directional forward diffusion of cells.^{23,24} Second, in the case of conventional dark-field microscopy (DF) with a Nikon condenser (0.8–0.9 NA) such as the one used in this work, the NA of the microscope objective will be limited to 0.7 NA. In the case of RLM, this limitation is removed and application of a 1.3 NA immersion objective with an additional narrow spectral range filter (545 ± 15 nm) for backscattering imaging provides high contrast between the NPs and the cells and allows precise 3D nanoparticle localization. The resulting typical experimental images of MDA-MB-231 cells decorated with 100 nm gold NPs obtained by RLM are presented in Fig. 2A. The corresponding real-time animation for 3D microscopy z-scan with a 200 nm step can be found in Video S1.† In Fig. S1(A and B)† we also

present a direct comparison of RLM with conventional transmission dark-field microscopy equipped with a dark field condenser (NA = 0.9, Nikon) and a 0.7 NA objective. A drastic contrast improvement for NP visualization in the cellular environment is obvious.

Experimental realization of the RLM method is very simple and can be easily combined with other microscopy modes. For example, the contrast of cells obtained by RLM is very low, and to facilitate the simultaneous visualization of cells with efficient NP targeting, the RLM imaging technique can be combined with oblique illumination mode. This mode results in 3D-like cell imaging (Fig. 2B), which in the case of fixed MB-231 cells can even help to detect the position of the cell nucleus (Fig. S1(C)†). Thus, the RLM mode for NP imaging is a basic part of our optical system, which provides accurate identification of the spatial position of NP markers and provides improved control over the choice of perforation points. In combination with another microscopy mode, it allows analysis and evaluation of the optical and mechanical kinetics of NPs and the dynamics of cellular responses. As an example, we present in Fig. 3A a reconstructed image of the spatial positions of individual NPs obtained by a 3D scan of the NP–cell complex using a consecutive 50 nm z-step. This scan allows choosing optoporation NPs that placed directly on the membrane and, importantly, estimation of NP cellular endocytosis. This particular sample of 100 nm NP–cell mix was prepared for 24 hours in an incubator before washing. As presented in the figure, more than 200 NPs were localized mostly on the cell membrane. By taking the 2D section from our 3D image we can estimate the quantity of NPs placed in the cell internal volume (Fig. 3B). Statistically, we obtained about 5% of internalized NPs after 24 hours of sample preparation. Experimental data show that after the usual 3 hours of sample preparation 100 nm gold NPs remain on the cell membrane and thus can be used for localized perforation. Even if NPs are inside the cell they can be detected by RLM 3D scan and removed from consideration.

Single cell optoporation experiments

The performance of controlled single point optoporation of a single live cell depends on the precision of the 3D spatial alignment of the laser focal point with the individual NP marker placed directly on the cell membrane. Both hardware and software algorithms have to be accurate while also being

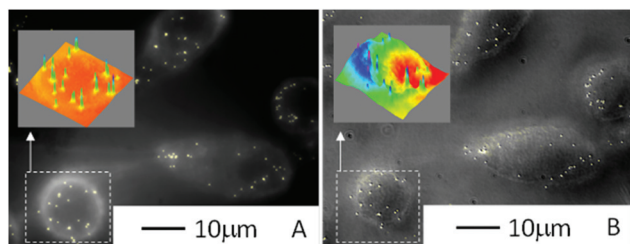


Fig. 2 (A) Wide-field RLM imaging of the NP–cell complex. (B) Imaging by using the method of oblique illumination and RLM.

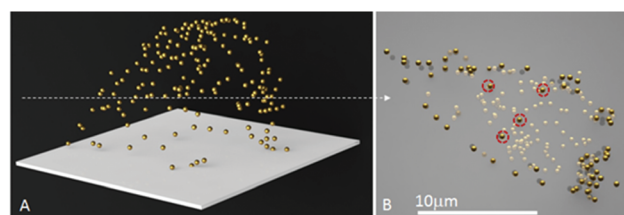


Fig. 3 (A) Spatial positions of individual NPs obtained by a 3D scan of the NP–cell complex. (B) The intersection plane shows the NP positions on the membrane and inside of the cell (ESI 3Dscan_NP_Cell.avi†).

reasonably fast and work automatically. According to the literature, the most accurate numerical algorithm in terms of both accuracy and precision for tracking small spherical NPs is a direct Gaussian fit to the intensity distribution. On condition of a high signal to noise (S/N) ratio (>10) and a proper imaging camera, this method could provide very high 2D precision – up to 2 nm.²⁵ In this work, we adopted the Gaussian algorithm to fit the NP intensity profile measured by the RLM approach. As this microscopy mode provides a high S/N ratio for 100 nm gold NP visualization (>60) and requires a high NA immersion objective with high magnification, precise detection of NP positions on a cell membrane is ensured. We expect similar performance for the detection of the initial laser focal spot spatial position. Experimentally, we replaced the Petri dish with a Si-wafer and performed fine z-scan (60 nm step) to find the laser beam 3D intensity distribution and x_0, y_0 focal point position. As NP visualization by RLM and determination of the laser focal position are done by the same optical setup in the same wavelength range (532 nm laser wavelength, 545 ± 15 nm filter used for RLM imaging), the influence of chromatic aberration, especially on the Z-position, is minimized.

The typical pulsed laser single point perforation protocol is as follows: custom made LabView software performs Gaussian fit for PSF of the chosen NP marker, finds the corresponding x, y, z positions and moves the translation stage to align NPs with the initial laser position x_0, y_0 for consecutive illumination. As we show in Fig. 4, the NP marker of choice is aligned with the laser for local cell membrane optoporation. We estimated the alignment precision in a 2D plane in about 40 nm (translation stage min step is 20 nm) using a $100\times$ 1.3 NA objective (66 nm interpixel distance on the imaging camera) and several automatic iterations of the alignment procedure (4–6).

We have found experimentally that the stability of the laser spot on the sample still suffers from mechanical vibrations even though the microscopy setup is built on an optical table. The live cell membrane is rather flexible and that contributes to the attached NP spatial instability. This effect has to be compensated by automatic 3D NP tracking performed by a continuous z-scan and Gaussian fit in 3D space, which we found quite efficient, but still time-consuming. For this reason, we decided to stay with a high NA objective for NP imaging and tracking

while decreasing the actual NA for laser beam focusing and illumination. In Fig. 4B, we present the experimental laser intensity profile obtained with laser beam filling the full objective aperture and for a beam diameter of 1.8 mm while the objective stays at 1.3 NA. The full width of the beam at half its maximum intensity (FWHM) was increased from 0.35 μm (black curve) to 0.7 μm (red curve) while a 200 nm misalignment resulted in only 20% power loss. Correspondingly, the laser beam focal depth was increased from 0.5 μm to 2.5 μm which greatly facilitated power adjustment during NP illumination.

Wide-field imaging of NP-mediated laser cell perforation

Different types of short-pulse lasers, such as femto – pico and nanosecond lasers, were successfully applied for plasmonic NP assisted cellular optoporation and transfection.^{26,27} Our proposed setup can be used with any of these lasers; however, in this work, we are considering the application of nanosecond pulsed lasers. Such laser technology is already advanced to the level where their size, affordability, and simplicity of use allow for simplified and fast commercialization and a wide area of application. Another reason for using ns-pulsed lasers is their emission wavelength range compatible with the resonance absorbance peak of gold plasmonic NPs. In this case, rather low power lasers can generate thermo-optical phenomena of the NP–laser interaction that leads to the optoporation of the cellular membrane.

As the first step, we have performed a series of experiments to investigate the phenomenon of the direct interaction between the nanosecond-laser and individual plasmonic NPs in a homogeneous medium. In this case, 100 nm AuNPs were deposited directly on the glass substrate of a Petri dish filled with water and visualized by RLM using a $100\times$ 1.3 NA objective with additional $\times 1.5$ magnification. The obtained typical intensity distribution of the NP PSF is shown in Fig. 5A. After thorough alignment with the focal position of the laser, the NP was illuminated with one pulse of a 15 ns laser. No significant changes were observed up to 200 mJ cm^{-2} laser energy. Increasing the energy to 300 mJ cm^{-2} resulted in NP heating, melting and fragmentation that was confirmed by evaluation of the corresponding PSF of NPs (Fig. 5B). A further increase of laser power destroys the NPs and results in the local substrate

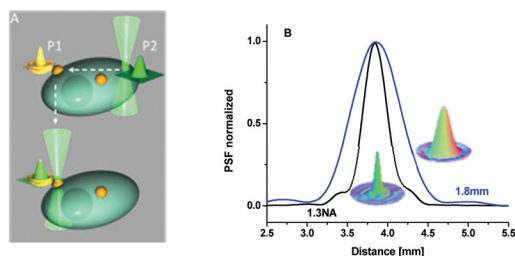


Fig. 4 (A) Alignment of the laser focal point with NP position. (B) Experimental laser intensity profile obtained with laser beam filling the full 1.3 NA objective aperture and for the beam with a diameter of 1.8 mm.

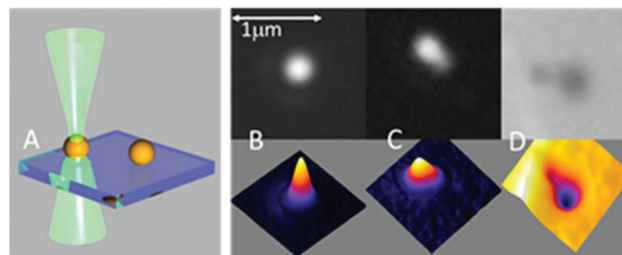


Fig. 5 (A) Ns-laser interaction with NPs placed on the glass surface. 2D and 3D point spread function of individual NPs obtained by RLM: (B) individual 100 nm Au NP on the glass substrate, (C) NPs after one pulse illumination with 300 mJ cm^{-2} power, and (D) NPs after one pulse illumination with 600 mJ cm^{-2} power.

ablation (Fig. 5C). The obtained results will help us to interpret and to optimize the conditions of NP-mediated laser cell perforation.

High contrast NP imaging and complementary membrane imaging by oblique illumination mode provided by our setup allow also the investigation of the optomechanical behavior of NP markers and the perforated membrane during laser-induced optoporation. Such phenomena depend on multiple parameters including laser power, NP–laser alignment precision, NP size and resonance properties, NP stage of aggregation and cellular medium. In Fig. 6 we present five typical scenarios of laser–NP interaction that were observed experimentally. A low energy laser ($<50 \text{ mJ cm}^{-2}$) generated no visible effect on the NP–cell complex. When the laser energy reaches 150 mJ cm^{-2} NP “low speed” response was detected and observed as slowly “sinking” in the z-direction (Fig. 6(A1 and A2)). Here we observed visually (Videos S2A and S2B†) and later confirmed by local fluorescence kinetics that “sinking” of NPs is related to the cell membrane perforation.²⁸ This effect can be explained by the local heating of NPs by the ns-laser and destruction of the membrane. When an energy of about 200 mJ cm^{-2} was applied an individual NP is displaced at a speed sufficiently low for conventional camera detection (10 frames per s). Such behavior is explained by the micro-bubble formation and explosion.²⁹ We believe that the generated NP displacing force is not sufficient for the 10 nm cellular membrane perforation, resulting in the lateral NP movement. A further increase in laser power ($300 \text{ mJ}–1.5 \text{ J cm}^{-2}$) was associated with enhanced NP heating, formation and explosion of bubbles¹³ and creation of pressure shock waves.¹¹ Experimentally, we observed NP fast disappearance by strong displacement or destruction and local cell membrane optoporation (Fig. 6(A3) and Video S2C†). For some cells, the pressure wave generated by laser–NP interaction caused an individual or even multiple bleb formation (Fig. 6(A5) and (B)). Increasing the laser power above 2 J cm^{-2} usually kills cells (Video S2C†). We verified experimentally that direct, no NPs mediated, illumination of cells with the same laser power had no impact on the cell membrane integrity, which confirms the resonance nature of NP-mediated perforation.

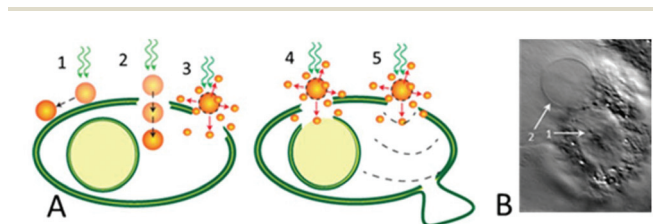


Fig. 6 Cell membrane–NP optomechanical phenomena after local perforation. (A1) The NP has displaced aside. (A2) The NP is “sinking”, producing local perforation. (A3) NP destruction and local cell membrane optoporation. (A4) Cell and nucleus membrane perforation. (A5) Pressure shock wave spreading and cell bleb formation. (B) An example of the cell bleb formation.

Analysis of perforation kinetics

In this work, we present an optical platform capable of performing cellular membrane perforation in a single point at the single cell level and of investigating the real-time cellular responses to the laser perforation procedure. Thus obtained results could provide essential information for the transfection protocol development and optimization.

As an example, we measured and analyzed perforation kinetics of PI inflow into an individual cell by detecting temporal and spatial fluorescence intensity distribution. Such analysis was performed by using human MDA-MB-231 cells seeded for 24 h prior to the experiment in glass-bottom dishes, labeled with 100 nm gold NPs and placed into an incubator installed on our platform. Spatial localization and energy of laser-induced optoporation were controlled automatically by using LabView software. Four typical perforation kinetics after NP-mediated laser optoporation using one 15 ns pulse at different energies were experimentally observed and are presented in Fig. 6. For example, typical results obtained at laser energies of $200–300 \text{ mJ cm}^{-2}$ are shown by a black curve. Fluorescence intensity kinetics presented by curve II corresponds to a laser energy level at $300–600 \text{ mJ cm}^{-2}$. Further increasing the laser power up to 1.5 J cm^{-2} resulted in dependence, shown as curve III, and finally, curve IV was obtained at energies higher than 2 J cm^{-2} . After optoporation tests with PI inflow, we performed cell viability assays using cell-permeant Calcein AM dye and measured the intensity of green-fluorescent calcein 1 hour after perforation.

We have found that up to 90% cells survive after low energy laser perforation (Fig. 7, curves I and II, Fig. 8B), whereas higher laser power kills cells (Fig. 7, curves III and IV). Analysis of the obtained experimental kinetics reveals two characteristic peaks (Fig. 7, lines 1 and 2). The first peak is related to the effect of the fast initial PI diffusion into the perforated membrane hole.³⁰ Then, after partial cell membrane repair³¹ and the photobleaching effect³² the measured PI fluo-

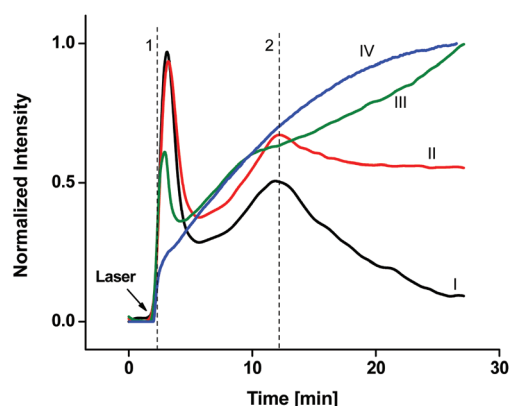


Fig. 7 Kinetics of propidium iodide inflow and propidium iodide–nucleic acid complex diffusion in MDA-MB-231 cells after gold nanoparticle-mediated optoporation. Curves I–IV correspond to the different laser energies. Normalized fluorescence intensity is presented on the Y-axis.

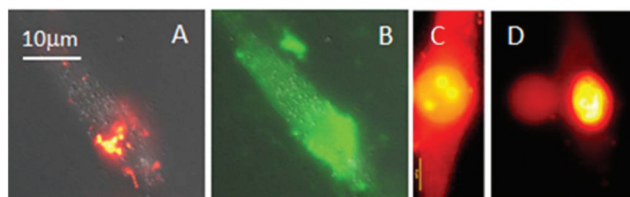


Fig. 8 (A) Fluorescence imaging of propidium iodide 30 min after laser optoporation. (B) Cell viability assays using cell-permeant Calcein dye. PI fluorescence imaging after nucleus staining (C) and after cell bleb formation (D). When the NP was placed close to the nucleus (Fig. 6(A4)) both the cell and nucleus membrane could be perforated.

rescence intensity decreased. A slow fluorescence intensity increase to the point of the second peak can be explained by the diffusion of much larger and slower PI-RNA/DNA complexes that were formed immediately after the inflow of PI within the cytoplasm. This peak, we think, is related to the moment of the disrupted plasma membrane recovery. After sealing the membrane hole several phenomena were observed. Firstly, the measured PI intensity gradually decreased due to photobleaching in the cytoplasm (curve I). We also observed a saturation effect on curve II, which can be explained by the existence of the external clusters that were ejected from the cell during perforation and could activate PI in the solution (Fig. 8A). High initial damage to the cell membrane initiates cell necrosis and PI reaches and stains the nucleus (Fig. 7, curves III and IV, Fig. 8C). As shown in Fig. 8D cell bleb formation can be also detected by fluorescence imaging.

In Fig. 7 we presented only normalized integral fluorescence intensity from one single cell. However, the developed system is equipped with high resolution imaging optics that, together with available 3D scan, allows measurements and analysis of temporal cellular responses locally, spatially, even providing a 3D spatiotemporal map. Such information is important and essential in the development of industrial laser-based transfection platforms.

We believe that the experimental optical setup presented in this work can be useful for quantitatively controlled delivery of different biomaterials to single cells in one point and for determining the dynamics of cellular reactions in real time. At the same time, this setup can give interesting results for direct laser-NP interaction in cell media. Consideration may be given to, for example, the dependence of cellular internalization of NPs on the size (>60 nm), time and surface functionalization of NPs, including NP-based drug delivery.

Conclusions

We demonstrated an optical setup and developed a methodology for automatic and accurate single-point single live cell NP-mediated laser optoporation with the possibility to analyze cell dynamics in real time. The accuracy of perforation of the cell membrane is ensured by reliable identification and accurate spatial localization of individual gold nanoparticles in the

cell medium using RLM. The resonance nature of NP-mediated perforation allows locally puncturing the cell membrane at a single point without damaging cells at the subcellular level. This system is based on an inverted microscopy setup and allows integration of additional microscopy modes, such as conventional transmission and fluorescence imaging. In this article, we presented examples of the spatiotemporal analysis of the responses of living cells to perforation events, which may be important for the quantitatively controlled delivery of various molecules into individual cells with precisely controlled insertion position at the cellular or subcellular level.

Conflicts of interest

There are no conflicts to declare.

Notes and references

- 1 D. G. Spiller, C. D. Wood, D. A. Rand and M. R. H. White, *Nature*, 2010, **465**, 736–745.
- 2 T. Fan-Gang and S. T. Subhra, *Essentials of Single-Cell Analysis. Concepts, Applications and Future Prospects*, Springer, Berlin, 2016.
- 3 W. M. Kang, F. Yavari, M. Minary-Jolandan, J. P. Giraldo-Vela, A. Safi, R. L. McNaughton, V. Parpoil and H. D. Espinosa, *Nano Lett.*, 2013, **13**, 2448–2457.
- 4 E. Y. Lukianova-Hleb, A. P. Samaniego, J. G. Wen, L. S. Metelitsa, C. C. Chang and D. O. Lapotko, *J. Controlled Release*, 2011, **152**, 286–293.
- 5 E. Boulais, R. Lachaine and M. Meunier, *Nano Lett.*, 2012, **12**, 4763–4769.
- 6 X. Chen, R. S. Leow, Y. X. Hu, J. M. F. Wan and A. C. H. Yu, *J. R. Soc., Interface*, 2014, **11**, 1–11.
- 7 T. K. Kim and J. H. Eberwine, *Anal. Bioanal. Chem.*, 2010, **397**, 3173–3178.
- 8 E. Boulais, R. Lachaine, A. Hatef and M. Meunier, *J. Photochem. Photobiol., C*, 2013, **17**, 26–49.
- 9 Y. T. Chow, S. X. Chen, R. Wang, C. C. Liu, C. W. Kong, R. A. Li, S. H. Cheng and D. Sun, *Sci. Rep.*, 2016, **6**, 1–9.
- 10 S. Kar, M. Loganathan, K. Dey, P. Shinde, H. Y. Chang, M. Nagai and T. S. Santra, *J. Micromech. Microeng.*, 2018, **28**, 1–24.
- 11 D. J. Stevenson, F. J. Gunn-Moore, P. Campbell and K. Dholakia, *J. R. Soc., Interface*, 2010, **7**, 863–871.
- 12 H. Georg Breunig, A. Uchugonova, A. Batista and K. Konig, *Sci. Rep.*, 2015, **5**, 11185.
- 13 Y. Arita, M. Ploschner, M. Antkowiak, F. Gunn-Moore and K. Dholakia, *Opt. Lett.*, 2013, **38**, 3402–3405.
- 14 M. Waleed, S. U. Hwang, J. D. Kim, I. Shabbir, S. M. Shin and Y. G. Lee, *Biomed. Opt. Express*, 2013, **4**, 1533–1547.
- 15 S. Patskovsky, E. Bergeron, D. Rioux and M. Meunier, *J. Biophotonics*, 2015, **8**, 401–407.

- 16 P. Zhang, S. Lee, H. Yu, N. Fang and S. H. Kang, *Sci. Rep.*, 2015, **5**, 11447.
- 17 S. L. Liu, J. C. Li, Z. L. Zhang, Z. G. Wang, Z. Q. Tian, G. P. Wang and D. W. Pang, *Sci. Rep.*, 2013, **3**, 1–5.
- 18 S. Lindstrom and H. Andersson-Svahn, *Lab Chip*, 2010, **10**, 3363–3372.
- 19 D. B. Chithrani, *Mol. Membr. Biol.*, 2010, **27**, 299–311.
- 20 B. D. Chithrani, A. A. Ghazani and W. C. W. Chan, *Nano Lett.*, 2006, **6**, 662–668.
- 21 S. L. Zhang, J. Li, G. Lykotrafitis, G. Bao and S. Suresh, *Adv. Mater.*, 2009, **21**, 419–424.
- 22 E. Oh, J. B. Delehanty, K. E. Sapsford, K. Susumu, R. Goswami, J. B. Blanco-Canosa, P. E. Dawson, J. Granek, M. Shoff, Q. Zhang, P. L. Goering, A. Huston and I. L. Medintz, *ACS Nano*, 2011, **5**, 6434–6448.
- 23 R. A. Meyer, *Appl. Opt.*, 1979, **18**, 585–588.
- 24 Q. Zhang, L. Zhong, P. Tang, Y. Yu, S. Liu, J. Tian and X. Lu, *Sci. Rep.*, 2017, **7**, 1–10.
- 25 M. K. Cheezum, W. F. Walker and W. H. Guilford, *Biophys. J.*, 2001, **81**, 2378–2388.
- 26 Z. P. Qin and J. C. Bischof, *Chem. Soc. Rev.*, 2012, **41**, 1191–1217.
- 27 D. Lapotko, *Opt. Express*, 2009, **17**, 2538–2556.
- 28 M. Li, T. Lohmuller and J. Feldmann, *Nano Lett.*, 2015, **15**, 770–775.
- 29 E. Lukianova-Hleb, Y. Hu, L. Latterini, L. Tarpani, S. Lee, R. A. Drezek, J. H. Hafner and D. O. Lapotko, *ACS Nano*, 2010, **4**, 2109–2123.
- 30 S. Kalies, G. C. Antonopoulos, M. S. Rakoski, D. Heinemann, M. Schomaker, T. Ripken and H. Meyer, *PLoS One*, 2015, **10**, 1–20.
- 31 Z. Z. Fan, H. Y. Liu, M. Mayer and C. X. Deng, *Proc. Natl. Acad. Sci. U. S. A.*, 2012, **109**, 16486–16491.
- 32 Y. A. Lau, B. L. Henderson, J. Lu, D. P. Ferris, F. Tamanoi and J. I. Zink, *Nanoscale*, 2012, **4**, 3482–3489.